J. Inst. Eng. India Ser. C (April 2018) 99(2):139–150
https://doi.org/10.1007/s40032-016-0325-y

ORIGINAL CONTRIBUTION

A Study on Tooling and Its Effect on Heat Generation and Mechanical Properties of Welded Joints in Friction Stir Welding

Sujoy Tikader[1] · Pankaj Biswas[1] · Asit Baran Puri[2]

Received: 27 March 2015 / Accepted: 25 May 2016 / Published online: 23 June 2016

Abstract Friction stir welding (FSW) has been the most attracting solid state welding process as it serves numerous advantages like good mechanical, metallurgical properties etc. Non weldable aluminium alloys like 5XXX, 7XXX series can be simply joined by this process. In this present study a mathematical model has been developed and experiments were successfully performed to evaluate mechanical properties of FSW on similar aluminium alloys i.e. AA1100 for different process parameters and mainly two kind of tool geometry (straight cylindrical and conical or cylindrical tapered shaped pin with flat shoulder). Tensile strength and micro hardness for different process parameters are reported of the welded plate sample. It was noticed that in FSW of similar alloy with tool made of SS-310 tool steel, friction is the major contributor for the heat generation. It was seen that tool geometry, tool rotational speed, plunging force by the tool and traverse speed have significant effect on tensile strength and hardness of friction stir welded joints.

Keywords Friction stir welding · Stirring effect · TMAZ · Process parameters · Tool geometries · Experimental investigation · Thermal analysis

✉ Sujoy Tikader
sujoytikader1987@gmail.com

[1] Indian Institute of Technology Guwahati, Guwahati 781039, Assam, India

[2] National Institute of Technology Durgapur, Durgapur 713209, West Bengal, India

List of symbols

AA	Aluminium alloy
$\left[C_e^t\right]$	Element specific heat matrix
FSW	Friction stir welding
HAZ	Heat affected zone
H_P	Height of the probe
h_1	Indent height of shoulder
h_f	Convection coefficient
$\left[K_e^{tb}\right]$	Element diffusion conductivity matrix
$\left[K_e^{tc}\right]$	Element convection surface conductivity matrix
$\{L\}$	Vector operator
$\{N\}$	Element shape function
$\{n\}$	Unit outward normal vector
P_n	Plunging force
Q_{Sp}	Heat generation due to vertical pressure in shoulder
Q_{Sm}	Heat generation in shoulder due to travelling of tool shoulder
Q_S	Total heat generation in shoulder
Q_1	Heat generation due to vertical pressure at probe tip
Q_2	Heat generation due to the rotational movement of the probe (side surface)
Q_3	Heat generation due to travelling of the probe (side surface)
Q_P	The total heat generation at the probe
$\left\{Q_e^f\right\}$	Element heat flow vector for surface S_1
$\left\{Q_e^c\right\}$	Elemental convection surface heat flow vector
q_{sup}	Heat supply
q'''	Heat generation
$\{q\}$	Heat flux vector
R_S	Shoulder radius
R_{Pb}	Radius of probe base
R_{Pt}	Radius of probe tip
S_{ys}^*	The yield strength of the material at 80 % of the melting point temperature

T_α	Ambient temperature
$\{T_e\}$	Nodal temperature vector
V	Tool velocity
ω	Angular velocity of the tool
τ^*	The shear strength of the material at 80 % of its melting point temperature
μ	Frictional co-efficient between the tool and workpiece
ρ	Density of plate material

Introduction

Friction stir welding involves the joining of metals without fusion or filler materials. It is a solid–state joining process that takes place below the melting point of the materials to be joined. The maximum temperature reached was generally of the order of 0.8 of the liquidus temperature of the material being welded. This welding process was invented at The Welding Institute, UK in the early 90's [1]. The welds were created by the combined action of frictional heating and mechanical deformation due to a rotating tool. Welds produced by FSW generally exhibits a higher strength and formability due to the low welding temperatures compared to fusion welding processes [2, 3]. FSW can potentially replace the riveting and resistance spot welding of aluminum and steel sheets in the aircraft and automotive industries, respectively [4]. Friction stir welding has been widely researched in marine and aerospace application because it is thought to be the appropriate technique without defects [5], which may occur in arc welding of aluminum alloys. The disadvantageous effects of arc welding like very high localized heating beyond the melting temperature, residual stresses and deformations are minimized in FSW, as the heat generated is less than the melting point of base plate. In marine application, marine grade steel is generally used for haul and superstructures. But aluminum has become a very good choice as it is lightweight, and allows for minimal rusting of aluminum to take place as compared to steel. The geometrical effect of FSW tool on welding quality [6–10] is a crucial part of this welding process. Some authors analyzed the influence of the tool rotation speed [11, 12], welding speed [13–16] and both parameters simultaneously [17–22] of 7XXX, 6XXX and 5XXX welds by considering the same tool geometry. They observed that different rotational speeds did not result in significant differences in the hardness profile in FSW welds, except for the width of the softened region in the weld of 6063-T5 Al. They suggested that frictional heat and plastic flow of plasticized material [23] during friction stir welding created fine and equiaxed [16] grains in the stir zone, and elongated and recovered grains in the Thermo-mechanically affected zone (TMAZ).The aim of the present study is to investigate the effect of process parameters [24, 25] viz. tool geometry, plunging force and rotational speed of the tool on mechanical properties [26–29] of similar friction stir butt welds AA1100.

Model Methodology

Let us consider a cylindrical tool whose shoulder radius is R_S and radius of its probe is R_{Pt}, whereas, considering height of the probe as H_p as shown in Fig. 1. If the angular speed of the tool is considered as ω and it is given a plunging force P_n due to which a pressure P is generated by the tool on the shoulder surface, due to this pressure the generation of total heat is calculated as follows.

An elemental ring of thickness δr is taken which is at r distance away from the centre O shown in Fig. 2. Then the area of the elemental ring will be,

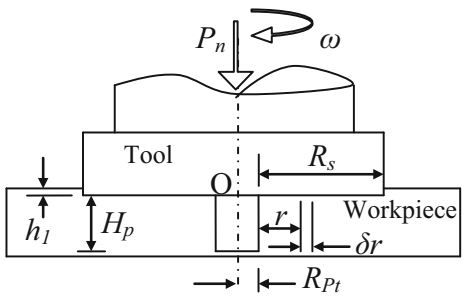

Fig. 1 Schematic diagram of flat cylindrical shoulder and cylindrical probe

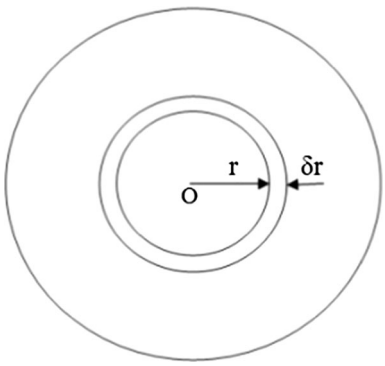

Fig. 2 Shoulder small elementary area

$$\delta A = 2\pi r \delta r \tag{1}$$

Normal force acting on this elemental ring,

$$\delta N = P \cdot \delta A = P \cdot 2\pi r \delta r \tag{2}$$

If one considers the frictional co-efficient between the tool and workpiece to be μ, the frictional force will be,

$$\delta F = \mu \cdot \delta N = 2\mu P \pi r \delta r \tag{3}$$

Heat generation due to elemental ring,

$$\delta Q_{Sp} = \delta F \times V_t = 2\mu P \pi r \delta r \cdot \omega r \tag{4}$$

where V_t is the tangential velocity. Integrating both sides of Eq. (4) one gets,

$$Q_{Sp} = 2\pi\mu\omega P \int_{R_{Pt}}^{R_S} r^2 \delta r$$

or

$$Q_{Sp} = \frac{2}{3}\pi\mu\omega P\left(R_S^3 - R_{Pt}^3\right) \tag{5}$$

Let us consider the depth by which the tool shoulder penetrate the work plate due to plunging force in welding area, is h_1 and the tool moves with a velocity of V. Now the yield strength of the material at 80 % of the melting point temperature is considered as S_{ys}^*. Since the tool is moving forward with a traverse velocity then one force will act upon the front half curved surface area of the shoulder. The area responsible for heat generation,

$$A = \pi R_S \cdot h_1 \tag{6}$$

Frictional force which is responsible for heat generation is,

$$F = \mu S_{ys}^* \cdot A = \mu\pi S_{ys}^* R_S h_1 \tag{7}$$

Heat Generation

$$Q_{Sm} = F \times V = \mu\pi S_{ys}^* R_S h_1 V \tag{8}$$

So, the total heat generation,

$$Q_s = Q_{Sp} + Q_{Sm}$$

$$Q_s = \frac{2}{3}\pi\mu\omega P\left(R_S^3 - R_{Pt}^3\right) + \mu\pi S_{ys}^* R_S h_1 V \tag{9}$$

Heat Generation in Cylindrical Probe

There are two important surfaces of probe. These are responsible for heat generation i.e. (i) probe tip surface and (ii) probe side surface.

The details of mathematical models of heat generation [30, 31] both on probe tip and side surface are described below.

Heat Generation Due to Vertical Pressure at Probe Tip

Similar to Eq. (5),

$$Q_1 = \frac{2}{3}\pi\mu\omega P \cdot R_{Pt}^3 \tag{10}$$

Heat Generation due to the Rotational Movement of the Probe Side Surface

If one considers τ to be the shear strength of the workpiece and τ^* be the shear strength of the material at 0.8 of its melting point temperature, then the force acting on the probe on its surface will be,

$$F_p = \mu\tau^* \cdot 2\pi R_{Pt} H_P \tag{11}$$

Heat generation by the curved surface area,

$$Q_2 = 2\mu\pi\tau^*\omega R_{Pt}^2 \cdot H_P \tag{12}$$

Heat Generation Due Traverse Speed of the Tool by the Probe Side Surface

Let us assume that probe is moving with a velocity of V and the yield strength of the workpiece material at 0.8 of its melting temperature be S_{ys}^*. Here only half of the curved surface area is responsible for heat generation during the travelling of probe i.e.

$$A = \pi r H_P$$

Therefore, force acting on the probe due to travelling on workpiece is,

$$F_p = \mu S_{ys}^* \pi R_{Pt} H_P \tag{13}$$

Therefore heat generation due to travelling of probe on workpiece is,

$$Q_3 = \mu S_{ys}^* \pi R_{Pt} \cdot H_P \cdot V \tag{14}$$

So the total heat generation by the probe is calculated by adding Eq. (10), (12) and (14),

$$Q_p = Q_1 + Q_2 + Q_3$$

or,

$$Q_p = \frac{2}{3}\pi\mu\omega P \cdot R_{Pt}^3 + 2\mu\pi\tau^*\omega R_{Pt}^2 \cdot H_P + \mu S_{ys}^* \pi R_{Pt} \cdot H_P \tag{15}$$

Therefore, total heat generation by flat cylindrical shoulder with cylindrical probe is calculated by,

$$Q = Q_s + Q_p$$

or

$$Q = \frac{2}{3}\pi\mu\omega P\left(R_S^3 - R_{Pt}^3\right) + \mu\pi S_{ys}^* R_S h_1 V + \frac{2}{3}\pi\mu\omega P \cdot R_{Pt}^3 + 2\mu\pi\tau^*\omega R_{Pt}^2 \cdot H_P + \mu S_{ys}^* \pi R_{Pt} \cdot H_P \cdot V \quad (16)$$

Similarly, for flat cylindrical tool with conical pin the total heat generated can be calculated by the below mentioned equation,

$$Q = \frac{2}{3}\pi\mu\omega P\left(R_S^3 - R_{Pt}^3\right) + \mu\pi S_{ys}^* R_S h_1 V + \frac{2}{3}\pi\mu\omega P\left(R_S^3 - R_{Pt}^3\right) + \left\{\frac{2}{3}\pi\mu\omega\tau^*\left(R_{Pb}^2 + R_{Pb}R_{Pt} + R_{Pt}^2\right) + \frac{\mu}{2}\pi S_{ys}^* V(R_{Pb} + R_{Pt})\right\} \sqrt{(R_{Pb} - R_{Pt})^2 + H_P^2} \quad (17)$$

Heat Flux Calculation

Heat Flux in Cylindrical Shoulder

Heat flux (q) can be obtained by dividing Eq. (4) by Eq. (1)

$$\text{i.e.} \quad \frac{\delta Q_{Sp}}{\delta A} = \frac{2\mu\pi\omega P r^2 \delta r}{2\pi r \delta r} \quad (18)$$

or

$$q = \mu\omega \Pr \quad (19)$$

Multiplying and dividing Eq. (19) by $\frac{2}{3}\pi\left(R_S^3 - r_p^3\right)$, one gets,

$$q = \frac{\frac{2}{3}\mu\pi\omega P\left(R_S^3 - R_{pb}^3\right) r}{\frac{2}{3}\pi\left(R_S^3 - R_{pb}^3\right)} \quad (20)$$

Using Eq. (5),

$$q = \frac{3Q_{Sp} r}{2\pi\left(R_S^3 - R_{pb}^3\right)} \quad (21)$$

Heat flux due to travelling of shoulder

As the radius of shoulder is constant at the curved surface area therefore heat flux is taken as uniform. Heat generation is taking place at half of the depressing curved surface area which is given in Eq. (6).

Therefore heat flux can be calculated by using Eq. (8) as,

$$q = \frac{Q_{Sm}}{A} \quad (22)$$

Heat Flux in Probe

There are two important areas where flux is needed to be calculated (a) Curved surface area of the probe and (b) Tip of the probe.

For Curved Surface Area

Since radius of the probe is not changing the heat flux through curved surface area is taken as uniform. Curved surface area of the probe

$$A = 2\pi R_{Pt} H_P \quad (23)$$

Therefore heat flux is calculated as,

$$q = \frac{Q_2 + Q_3}{A} \quad (24)$$

where Q_2 and Q_3 are taken from Eq. (12) and (14).

For Tip of the Probe

Similar to Eq. (21),

$$q = \frac{3Q_1 r}{2\pi R_{Pb}^3} \quad (25)$$

Similarly one can calculate heat fFlux for conical shoulder and conical pin.

Experimental Procedure

Experimental Details

Two similar aluminium alloy of AA1100 grade test samples of size 200 mm long, 100 mm wide and 6 mm thick plates were welded with the below referred FSW tools. Specifications of milling machine used for FSW experimentation are vertical type milling machine, motor capacity: 7.5 HP, rotational Speeds: 50–1500 rpm, traversing speeds: 22–555 mm/min. The tool was rigidly fixed on an arbor. The workpiece edges are clamped to the machine bed without any root gap to restrict the movement in all degrees of freedom to with stand mainly plunging and translational forces of the tool. The butting line of two workpieces was seen to match exactly with the center of the tool pin. After allowing the tool to plunge on the butted plate and visually ensuring full contact of the tool shoulder with the plate surface, the bed horizontal movement was switched on and continued up to the end. A typical FSW setup is shown in Fig. 3. For measurement of tool plunging force a 5000 kg capacity load pad was used. Agilent data logger 34,970 A was used to record temperature data. The FSW tools were fabricated in house using SS310 shown in Fig. 4.

Four flat shouldered but different pin dimensioned FSW tools have been used in this work. Two are of flat shouldered straight cylindrical pin tool and other two are flat shouldered tapered cylindrical pin shown in Fig. 4. The FSW tools were fabricated in workshop using SS-310.

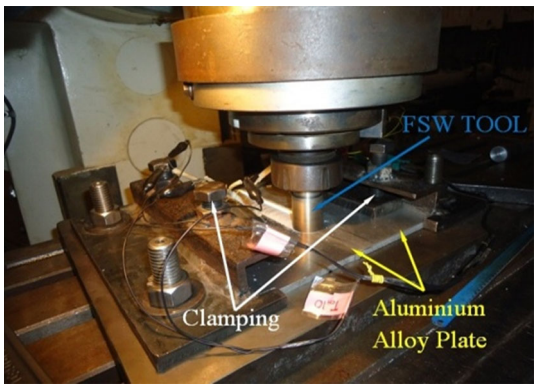

Fig. 3 Friction stir welding setup

Fig. 4 Conical tools (*top*) and cylindrical tools (*bottom*)

With the constant traverse speed of 112 mm/min and zero tool inclination angle the plunging forces are taken as 5100 and 6500 N in case of 1400 and 1000 rpm tool rotational speed respectively, for FSW of AA1100 grade.

Vickers Micro Hardness Test

Procedure to measure material's resistance to localized plastic deformation is done through hardness test. Required hardness value can vary depending upon the application and purpose of use. So to calculate the actual hardness value of welding zone compared to other zone of the welded plate, the test samples were made to carried micro hardness test which have been carried out on a Vickers micro hardness testing machine (Make BUEHLER, model no: 1600-6036, loading range: 10–2000 gf). Hardness measurements were taken on cross-sections perpendicular to the welding direction. Welding was carried out using four types of FSW tools with varying process parameters as shown in Table 1.

The hardness at the different zones of the test samples was measured. At a particular location on the weld zone ten number of hardness reading have been noted and the average of these readings was taken. The indentation load for the hardness measurement was kept at 100 gf. The variation of hardness value for all the eight test samples is shown in Fig. 5.

Table 1 Different process parameters used for similar FSW of AA1100

Exp. no.	Tool pin geometry	Tool pin diameter (mm)	Rotational speed of tool (rpm)
1	SC	5	1000
2	SC	6	1000
3	SC	5	1400
4	SC	6	1400
5	TC	5	1000
6	TC	6	1000
7	TC	5	1400
8	TC	6	1400

AA aluminium alloy, *S* straight, *T* tapered, *C* cylindrical)

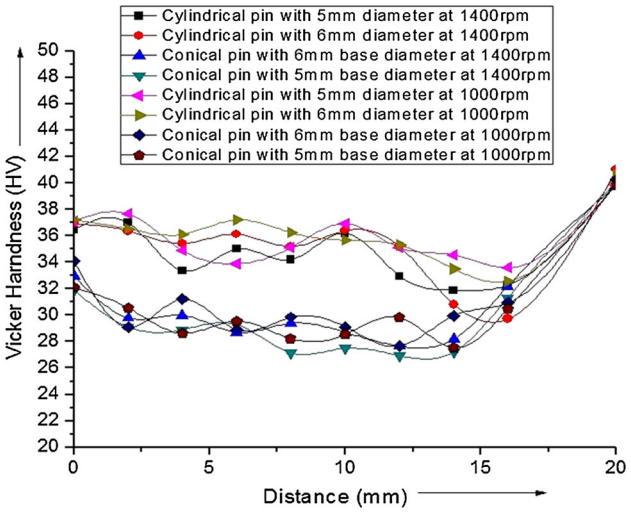

Fig. 5 Vickers micro hardness for eight different FSW samples

Tensile Test

As strength of any structure or a body is determined by its load carrying capacity so to quantify the strength or toughness or yield strength of the welded joint, tensile test was carried out and specimens were prepared after welding as per ASME standard and tensile tests have been carried out for the job specimens with 1400 rpm and 5100 N plunging force. Instron-8801 tensile testing machine was used for tensile test. The specifications of this machine are closed loop servo hydraulic dynamic testing machine, maximum load capacity is 100 kN, and actuator displacement is about 75 mm and in full scale 150 ± 5 mm.

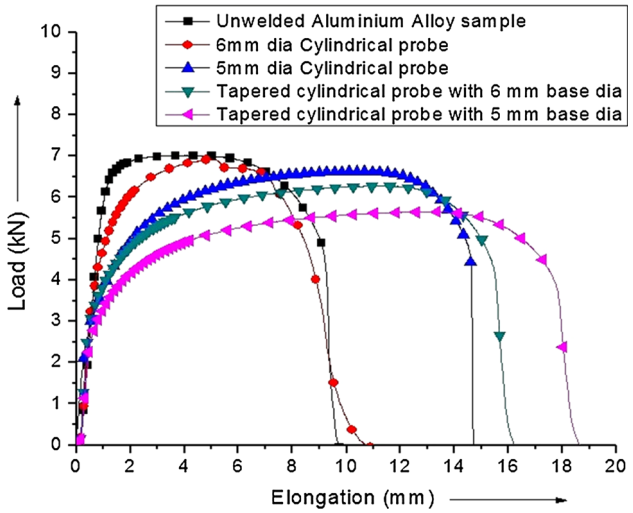

Fig. 6 Load versus elongation plot for four samples welded by different tool geometry for same process parameters

The tensile test specimens were taken perpendicular to the welding direction from the welded test samples. All tensile tests were performed at a constant crosshead displacement rate of 4 mm/min using an Instron tensile testing machine. Tests were performed to study the load versus elongation characteristics for the specimens welded under different parameters. Load versus elongation curves were plotted for the all the four samples welded under 1400 rpm and 5100 N plunging force have shown in Fig. 6. In this result, specimens 1 and 2 were welded by the cylindrical pin tool and the specimens 3 and 4 were welded with the tool of tapered pin geometry. It is observed that the load versus elongation plots of specimen 3 and 4 have enhanced nature compared to all others. It can be shown that the ultimate tensile strength for the specimens 3 and 4 were 30 % higher than the specimens 1 and 2.

Numerical Thermal Analysis

Three-Dimensional Finite Element Modeling [32, 33]

A three dimensional finite element transient thermal model was developed in the present work to analyze the heat transfer and temperature distribution in a FSW process. In the thermal model the actual conditions were accommodated as far as possible. The following assumptions were made in developing the present thermal model of a FSW process.

1. All the thermal properties were considered as function of temperature.
2. Linear Newtonian convection cooling was considered on all the surfaces.
3. Heat generation was considered as a load.

The governing differential equation is:

$$\frac{\partial}{\partial x}\left[K\frac{\partial T}{\partial x}\right]+\frac{\partial}{\partial y}\left[K\frac{\partial T}{\partial y}\right]+\frac{\partial}{\partial z}\left[K\frac{\partial T}{\partial z}\right]+q'''=\rho C\frac{\partial T}{\partial t} \tag{26}$$

where $\frac{\partial}{\partial x}\left[K\frac{\partial T}{\partial x}\right]$ = variation of heat flux in X direction, $\frac{\partial}{\partial y}\left[K\frac{\partial T}{\partial y}\right]$ = variation of heat flux in Y direction, $\frac{\partial}{\partial z}\left[K\frac{\partial T}{\partial z}\right]$ = variation of heat flux in Z direction, q''' = heat generation, ρ = density of plate material, C = specific heat and K = thermal conductivity.

The following boundary conditions were applied in the present FE model.

Equation (26) can be written as:

$$\rho c\frac{\partial T}{\partial t}=-\{L\}^T\{q\} \tag{27}$$

where $\{L\}=\begin{Bmatrix}\frac{\partial}{\partial x}\\ \frac{\partial}{\partial y}\\ \frac{\partial}{\partial z}\end{Bmatrix}$ = vector operator, $\{q\}$ = heat flux vector.

$$\{L\}^T\{q\}=\nabla\cdot\{q\}\ \text{and}\{L\}^T=\nabla T$$

where $\nabla.$ represents divergence operator and ∇ represents grad operator.

Fourier's law is used to relate the heat flux vector to the thermal gradient

$$\{q\}=-[D]\{L\}^T$$

where $[D]=\begin{bmatrix}K&0&0\\0&K&0\\0&0&K\end{bmatrix}$ = conductivity matrix.

Equation (27) can be written as:

$$\rho c\frac{\partial T}{\partial t}=\{L\}^T\left([D]\{L\}^T\right) \tag{28}$$

Boundary Conditions

Initial Condition

A specified initial temperature for the line heating that covers all the elements of the specimen $=T_\alpha$ for $t=0$, where T_α = the ambient temperature

To develop second and third boundary conditions one should consider energy balance at the work surface as:

Heat supply = Heat loss

First Boundary Condition

A specific heat flow acting over surface S_1

$$q_n = -q_{sup}$$

or

$$-K\frac{\partial T}{\partial n} = h_f(T - T_\alpha) \quad \text{for } t > 0 \tag{29}$$

The quantity q_n represents the component of the conduction heat flux vector normal to the work surface. The quantity q_{sup} represents the heat flux supplied to the work surface in $\frac{\mathrm{W}}{\mathrm{m}^2}$, from an external welding arc.

$$q_n = \{q\}^T\{n\} \tag{30}$$

on the surface S_1 for $t > 0$, where $\{n\}$ = unit outward normal vector.

Second Boundary Condition

Considering heat loss (q_{conv}) due to convection over surface S_2 (Newton's law of cooling):

$$q_n = q_{conv}$$

or

$$\{q\}^T\{n\} = h_f(T - T_\alpha) \tag{31}$$

on surface S_2 for $t > 0$.

Pre-multiplying Eq. (28) by a virtual change in temperature, integrating over the volume of the element, combining with Eqs. (30) and (31), and with some algebraic manipulation one gets:

$$\int_{vol}\left(\rho c\delta T\left(\frac{\partial T}{\partial t}\right) + \{L\}^T(\delta T)([D]\{L\}T)\right)d(vol) = \int_{S_1}\delta T q_{sup}d(S_1) + \int_{S_2}\delta T h_f(T_\alpha - T)d(S_2) \tag{32}$$

where vol = volume of the element, δT = an allowable virtual temperature $(= \delta T(x, y, z, t))$.

As stated before, the variable T is allowed to vary both in space and time. This dependency is expressed as:

$$T = \{N\}^T\{T_e\} \tag{33}$$

where $T = T(x, y, z, t)$ = Temperature, $\{N\} = \{N(x, y, z)\}$ = element shape function, $\{T_e\} = \{T_e(t)\}$ = nodal temperature vector.

The time derivatives of Eq. (33) may be written as:

$$\dot{\mathrm{T}} = \frac{\partial T}{\partial t} = \{N\}^T\{T_e\} \tag{34}$$

δT has the same form as T:

$$\delta T = \{\delta T_e\}^T\{N\} \tag{35}$$

The combination of $\{L\}T$ is written as:

$$\{L\}T = [B]\{T_e\}$$

where

$$[B] = \{L\}\{N\}^T \tag{36}$$

The variational statement of Eq. (32) can be combined with Eqs. (33), (34), (35) and (36) to yield:

$$\int_{vol}\rho c\{\delta T_e\}^T\{N\}\{N\}^T\{\dot{\mathrm{T}}_e\}d(vol) + \int_{vol}\{\delta T_e\}^T\{B\}^T[D][B]\{T_e\}d(vol) = \int_{S_1}\{\delta T_e\}^T\{N\}q_{sup}d(S_1) + \int_{S_2}\{\delta T_e\}^T\{N\}h_f\left(T_\alpha - \{N\}^T\{T_e\}\right)d(S_2) \tag{37}$$

The density ρ is assumed to remain constant and specific heat C may vary over the element. Finally $\{T_e\}$, $\{\dot{\mathrm{T}}_e\}$ and $\{\delta T_e\}$ are nodal quantities and do not vary over the element, so that they also may be taken out from the integrals. Now, since all quantities are pre-multiplied by $\{\delta T_e\}$ this term may also be dropped from the resulting equation. Thus Eq. (37) may be reduced to:

$$\left[C_e^t\right]\{\dot{\mathrm{T}}_e\} + \left(\left[K_e^{tb}\right] + \left[K_e^{tc}\right]\right)\{T_e\} = \left\{Q_e^f\right\} + \left\{Q_e^c\right\}$$

which is used for solving thermal analysis in ANSYS software.

Where $\left[C_e^t\right] = \rho\int_{vol} c\{N\}\{N\}^T d(vol)$ = element specific heat matrix, $\left[K_e^{tb}\right] = [B]^T[D]\ [B]d(vol)$ = element diffusion conductivity matrix, $\left[K_e^{tc}\right] = \int_{S_2} h_f[N]\ [N]^T\ d(S_2)$ = element convection surface conductivity matrix, $\left\{Q_e^f\right\} = \int_{S_1}\{N\}q_{sup}d(S_1)$ = element heat flow vector for surface S1, $\left\{Q_e^c\right\} = \int_{S_2} T_\alpha\ \{N\}h_f d(S_2)$ = element convection surface heat flow vector.

This can be used for easily calculating temperature $\{T_e\}$.

Heat Source Modeling [34–40]

The input of heat is assumed to be linearly proportional to the radial distance from the center of the tool which is derived from the supposition (a) due to downward force on the workpiece by the tool creates a uniform pressure between the shoulder and the workpiece, and (b) from the work done by

Table 2 Temperature dependent material properties of Aluminum used in FE analysis

Temperature (°C)	Thermal conductivity (W/m °C)	Heat capacity (J/Kg °C)
37.8	162	945
93.3	177	978
148.9	184	1004
204.4	192	1028
260	201	1052
315.6	207	1078
371.1	217	1104
426.7	223	1133

Table 3 Temperature dependent friction coefficient of aluminum and steel

Temperature (°C)	Friction coefficient (μ)
22	0.11
160	0.11
200	0.26
400	0.35
580	0.47

the frictional effect between tool-workpiece interface the heat is generated. The distribution of the rate of heat flux to work piece can then be represented as shown in Eq. (38).

$$q(r) = \frac{3Qr}{2\pi r_0^3} \quad \text{for } r \leq r_0 \tag{38}$$

where r_0 = outside radius of the shoulder of the tool, Q is the rate of heat input to the work piece.

The distribution of heat flux over the pin-plate interface due to tool pin side surface is given by,

$$q_p = \frac{Q_p}{(A)_{ps}} \tag{39}$$

where $(A)_{ps}$ = The area of tool pin side surface.

Table 2 shows the temperature dependent material properties of aluminum alloy [41, 42] used for the transient heat transfer analysis. Constant convection co-efficient (i.e. 30 W/m^2 °C) was used [43] in the analysis. The melting point of commercial grade aluminum alloy is about 660 °C. Table 3 shows the temperature dependent friction coefficient of aluminum and steel [41, 42] used for the transient heat transfer analysis. The recrystallization temperature range of commercial grade aluminum alloy is generally 325–290 °C.

FE Results and Discussions

For calculation of weld induced frictional heat the vertical force first considered was obtained from published literature. It was seen the vertical force varied with welding speed. The vertical force obtained from published results is given in Table 4. In this present FE model the vertical plunging force considered with different welding parameters is shown in Table 4.

Table 4 Vertical plunging force on FSW tool and welding speed

Thickness of the plate (mm)	Rotational speed of tool (rpm)	Traverse speed (mm/min)	Average plunging force on FSW tool during welding (N)
6.0	1000	112	6500
6.0	1400	112	5100

Table 5 Process parameters upon which the experimental and numerical results are comprised

Plates thickness (mm)	Rotational speed (rpm)	Traverse speed (min/s)	Probe diameter (mm)
6	1400	112	6

Analysis of the results (Results and Discussion)

Vickermicro hardness test

From Vicker Micro Hardness Test results (Fig. 5) it is shown that the hardness value of the weld nugget is lower than the base materials because of the stirring effect of the pin with huge mechanical deformation, grain refinement [44] happens around the pin. So ductility improves of that zone due to which hardness decreases. It is seen that there is not much difference in the hardness values of weld zone and heat affected zone (HAZ).

Tensile Test

The tensile testing results shows (Fig. 6) that toughness for the welding sample welded by tapered cylindrical tool pin is more compared to straight cylindrical tool pin because area under the curve is greater here (Fig. 6), and the displacement before failure is more for tapered cylindrical tool compared to straight cylindrical tool of same base diameter (Table 5).

Verification of Numerical Analysis with Experimental Result

From the numerical and the experimental study it can be seen the both the result has come more or less same and the error between them is very less.

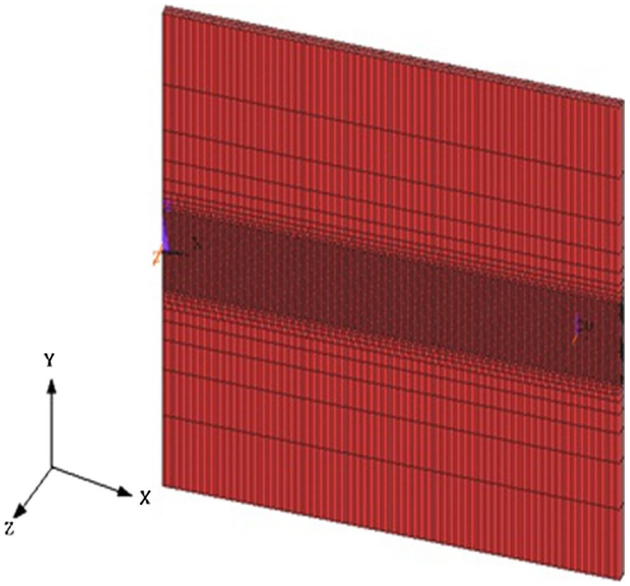

Fig. 7 FE model and meshing view

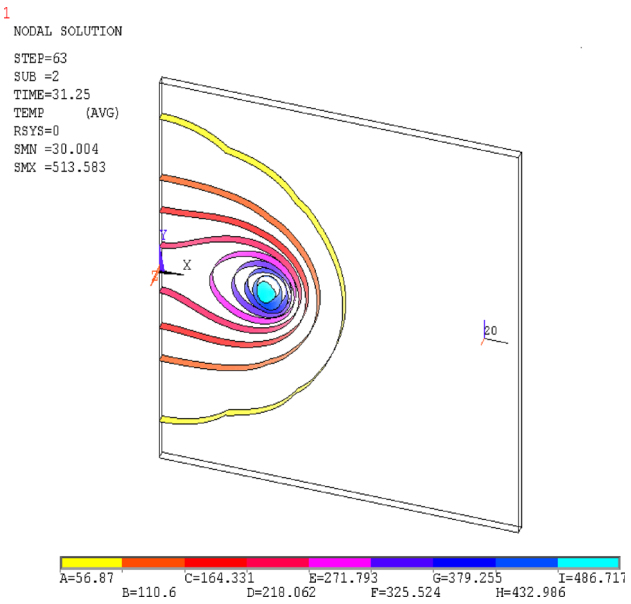

Fig. 8 Isothermal pattern for a particular time step during welding for 6 mm tapered pin diameter

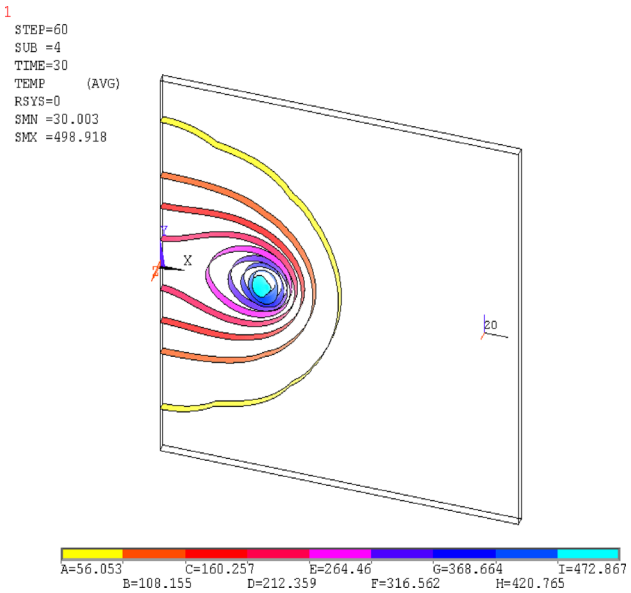

Fig. 9 Isothermal pattern for a particular time step during welding for 5 mm pin diameter

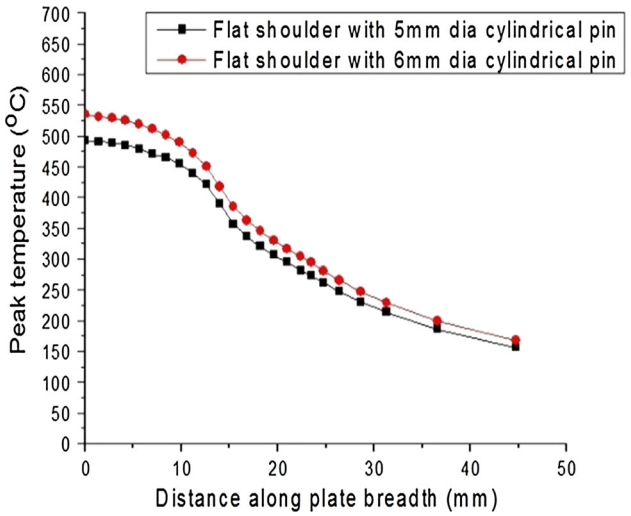

Fig. 10 Peak temperature distributions along plate breadth perpendicular to the weld line using conical pin

Figures 7, 8, 9, 10, 11 and 12 are showing mesh generation model and different numerical results based on FE model. It is understood from Figs. 10 and 11 that the heat generation is maximum at the weld nugget zone due to huge mechanical deformation arising from shear deformation as a result of traverse speed and frictional heating and decreases gradually with increase of the shoulder radius of the tool.

By numerical model the isotherm pattern can be seen from Figs. 8 and 9 at the time of welding. Like if one considers the peak temperature error calculation, then it can be seen from Fig. 13 that in experimental result it is approximately 494 °C and numerically it is 480 °C which leads to the maximum error of 2.91 %.

Conclusion

In this work 6 mm thick commercial grade aluminum plates have been welded by using 4 different types of tool(two straight cylindrical and two tapered cylindrical).

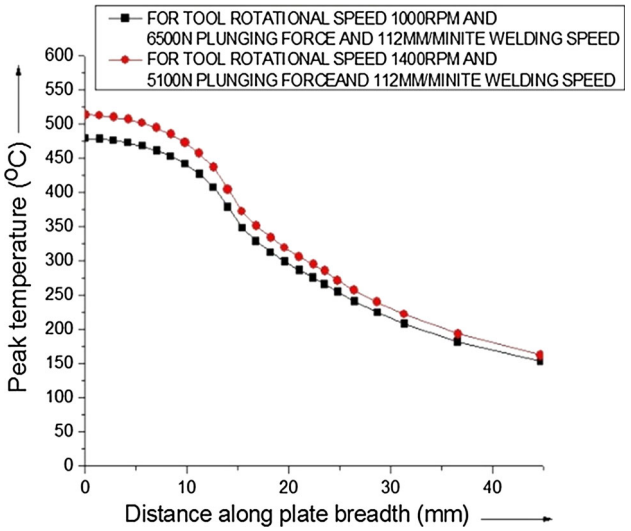

Fig. 11 Comparison of peak temperature distribution with distance perpendicular to the weld line for varying welding parameters

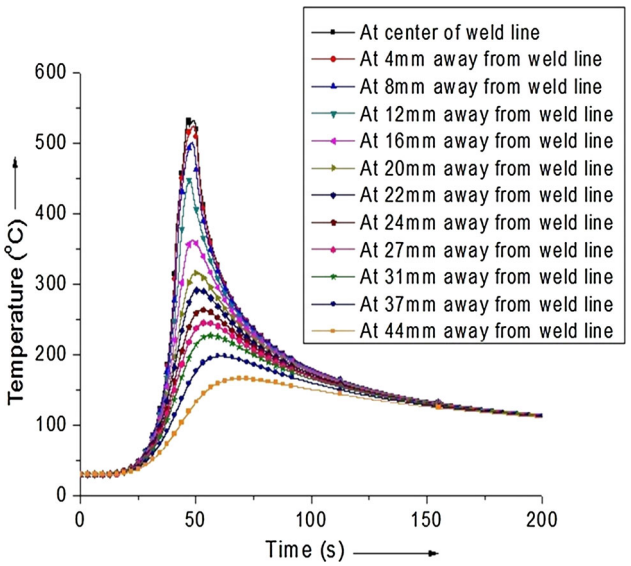

Fig. 12 Temperature distribution from center of weld line to away from weld line for 6 mm cylindrical probe diameter and flat circular shoulder frictional surface where the tool rotational and transverse speed were 1400 rpm and 112 mm/min respectively

From the above designed FSW tool geometry and the above process parameters, a very good quality weld has been achieved by which the following conclusions can be made:

a) The hardness value is more in case of straight cylindrical tool pin than tapered cylindrical tool pin for the same process parameters.
b) The average hardness value of the weld nugget zone reduces near about 13.28 % compared to base metal or parent metal zone.

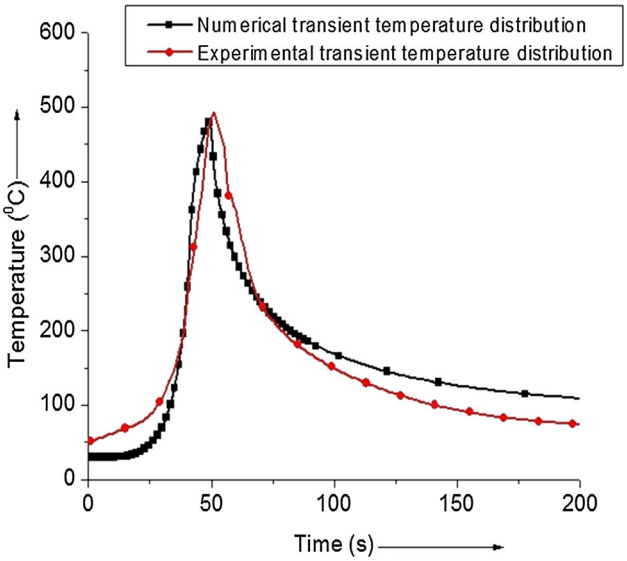

Fig. 13 Numerical and experimental comparison of temperature distribution at 5 mm away from center of weld line

c) It is observed that the tool with tapered pin profile generate less temperature than the tool with straight cylindrical pin profile.
d) For a particular welding parameter the increase in peak temperature for increment of 1 mm diameter in case of cylindrical pin was around 10 % only. Since increase in diameter does not significantly contribute to heat generation. It is preferable to keep the diameter as low as possible to avoid occurrence of wormhole defect.
e) Toughness was higher for welded sample done by tapered cylindrical tools with same process parameter because area under the curve is greater here as seen in tensile test.
f) The hardness values of the weld zone and HAZ are lower than the base material which indicates the improved ductility of the weld.

Acknowledgment This paper is the expanded version of an article titled, "A Study on Tooling and Its Effect on Heat Generation and Mechanical Properties of Welded Joints in Friction Stir Welding" presented in 5th International & 26th All India Manufacturing Technology, Design and Research Conference (AIMTDR 2014) during December 12–14, 2014 at Indian Institute of Technology Guwahati, India.

References

1. W.M. Thomas, E.D. Nicholas, J.C. Needham, M.G. Murch, P. Templesmith, C.J. Dawes, *Friction Stir Butt Welding*. International patent application No. PCT/GB92/02203 and GB patent application No. 9125978.8 (December 6, 1991)
2. J.Q. Su, T.W. Nelson, R. Mishra, M.W. Mahoney, Microstructural investigation of friction stir welded 7050-T651 alloy. Acta Mater. **51**(3), 713–729 (2003)

3. R.S. Mishra, Z.Y. Ma, Friction stir welding and processing. Mater. Sci. Eng. **50**, 1–78 (2005)
4. J. Sinke, M.M. Stofregen, E. Estraatsma, *Tailor Made Blanks for The Aircraft Industry: A Pilot Study*. Technical report (Netherlands Institute for Metals Research, 2005)
5. N.T. Kumbhar, K. Bhanumurthy, Friction stir welding of Al 6061 alloy. Asian J. Exp. Sci. **22**(2), 63–74 (2008)
6. W.M. Thomas, K.I. Johnson, C.S. Wiesner, Friction stir welding-recent developments in tool and process technologies. Adv. Eng. Mater. **5**, 485 (2003)
7. G. Buffa, J. Hua, R. Shivpuri, Mater. Sci. Eng., A **419**, 381–388 (2006)
8. K. Elangovana, V. Balasubramanianb, Influences of tool pin profile and welding speed on the formation of friction stir processing zone in AA2219 aluminium alloy. J. Mater. Process. Technol. **200**, 163–175 (2008)
9. P. Biswas, N.R. Mandal, Effect of tool geometries on thermal history of FSW of AA1100. Suppl. Weld. J. **90**, 129s–135s (2011)
10. H.K. Mohanty, M.M. Mahapatra, P. Kumar, P. Biswas, N.R. Mandal, Effect of tool shoulder and pin probe profiles on friction stirred aluminum welds—a comparative study. J. Mar. Sci. Appl. **11**, 200–207 (2012)
11. Y.S. Sato, M. Urata, H. Kokawa, Parameters controlling microstructure and hardness during friction-stir welding of precipitation-hardenable aluminum alloy 6063. Metall. Mater. Trans. A **33**(3), 625–635 (2002)
12. W. Tang, X. Guo, J.C. McClure, L.E. Murr, Heat input and temperature distribution in friction stir welding. J. Mater. Process. Manuf. Sci. **7**, 163–172 (1998)
13. W.B. Lee, Y.M. Yeon, S.B. Jung, Evaluation of the microstructure and mechanical properties of friction stir welded 6005 aluminum alloy. Mater. Sci. Technol. **19**(11), 1513–1518 (2003)
14. A. Simar, Y. Brechet, B. Meester, A. Denquin, T. Pardoen, Microstructure, local and global mechanical properties of friction stir welds in aluminum alloy 6005A-T6. Mater. Sci. Eng., A **486**(1/2), 85–95 (2008)
15. P. Cavaliere, A. De Santis, F. Panella, A. Squillace, Effect of welding parameters on mechanical and microstructural properties of dissimilar AA6082–AA2024 joints produced by friction stir welding. Mater. Des. **30**, 609–616 (2009)
16. T. Saeid, A. Abdollah-zadeh, H. Assadi, F. MalekGhaini, Effect of friction stir welding speed on the microstructure and mechanical properties of a duplex stainless steel. Mater. Sci. Eng., A **496**, 262–268 (2008)
17. M.J. Peel, A. Steuwer, P.J. Withers, T. Dickerson, Q. Shi, H. Shercliff, Dissimilar friction stir welds in AA5083–AA6082. Part I: process parameter effects on thermal history and weld. J. Mar. Sci. Appl. **12**: 493–499, 499 properties; Metall. Mater. Trans A **37**(7), 2183–2193 (2006)
18. S. Lim, S. Kim, C.G. Lee, S.J. Kim, Tensile behavior of friction-stir-welded Al 6061-T651. Metall. Mater. Trans. A **35**(9), 2829–2835 (2004)
19. P. Biswas, N.R. Mandal, Experimental study on friction stir welding of marine grade aluminum alloy. J. Ship Prod. **25**(1), 1–6 (2009)
20. M.J. Peel, A. Steuwer, P.J. Withers, Dissimilar friction stir welds in AA5083–AA6082. Part II: process parameter effects on microstructure. Metall. Mater. Trans. A **37**(7), 2195–2206 (2006)
21. S.R. Ren, Z.Y. Ma, L.Q. Chen, Effect of welding parameters on tensile properties and fracture behavior of friction stir welded Al–Mg–Si alloy. Scripta Mater. **56**(1), 69–72 (2007)
22. J.J. Muhsin, M.H. Tolephih, A.M. Muhammed, Effect of friction stir welding parameters (rotation and transverse) speed on the transient temperature distribution in friction stir welding of AA 7020-T53. ARPN J. Eng. Appl. Sci. **7**(4), 436–446 (2012)
23. K. Kumar, S.V. Kailas, The role of friction stir welding tool on material flow and weld formation. Mater. Sci. Eng., A **485**, 367–374 (2008)
24. J.H. Record, J.L. Covington, T.W. Nelson, C.D. Sorensen, B.W. Webb, A look at the statistical identification of critical process parameters in friction stir welding. Weld. J. **86**, 97s–103s (2007)
25. A.K. Lakshminarayan, V. Balasubramanian, Process parameters optimization for friction stir welding of RDE-40 aluminium alloy using Taguchi technique. Trans. Nonferrous Met. Soc. China. **18**, 548–554 (2008)
26. P.M.G.P. Moreira, T. Santos, S.M.O. Tavares, V. Richter-Trummer, P. Vilaça, P.M.S.T. de Castro, Mechanical and metallurgical characterization of friction stir welding joints of AA6061-T6 with AA6082-T6. Mater. Des. **30**, 180–187 (2009)
27. J. Adamowski, C. Gambaro, E. Lertora, M. Ponte, M. Szkodo, Analysis of FSW welds made of aluminium alloy AW6082-T6. Int. Sci. J. **28**(8), 453–460 (2007)
28. G. Cam, S. Gucluer, A. Çakan, H.T. Serindag, Mechanical properties of friction stir butt-welded Al-5086 H32 plate. J. Achiev. Mater. Manuf. Eng. **30**(2), 151–156 (2008)
29. A.K. Lakshminarayanan, V. Balasubramanian, An assessment of microstructure, hardness, tensile and impact strength of friction stir welded ferritic stainless steel joints. Mater. Des. **31**, 4592–4600 (2010)
30. C.M. Chen, R. Kovacevic, Finite element modeling of friction stir welding—thermal and thermo-mechanical analysis. Int. J. Mach. Tools Manuf **43**, 1319–1326 (2003)
31. N. Rajamanickam, V. Balusamy, Numerical simulation of transient temperature in friction stir welding of aluminum alloy 2014-T6 type. Manuf. Ind. Eng. (2), 41–44 (2007)
32. Mohamed Assidi, Lionel Fourment, S. Guerdoux, T. Nelson, Friction model for friction stir welding process simulation: calibrations from welding experiments. Int. J. Mach. Tools Manuf **50**, 143–155 (2010)
33. P. Heurtier, M.J. Jones, C. Desrayaud, J.H. Driver, F. Montheille, D. Allehaux, Mechanical and thermal modelling of friction stir welding. J. Mater. Process. Technol. **171**, 348–357 (2006)
34. O. Frigaard, O. Grong, O.T. Midling, Modeling of the heat flow phenomena in friction stir welding of aluminum alloys. in *Proceedings of the Seventh International Conference Joints in Aluminum—INALCO'98*, Cambridge, UK, 15–17 April 1998
35. O. Frigaard, O. Grong, O.T. Midling, A process model for friction stir welding of age hardening aluminum alloys. Metall. Mater. Trans. A. **32A**, 1189–1200 (2001)
36. O. Frigaard, O. Grong, B. Bjorneklett, O.T. Milding, *Modeling of the thermal and microstructure field during friction stir welding of aluminum alloys.1st International Symposium on Friction Stir Welding* (Thousand Oaks, Calif, 1999)
37. M. Song, R. Kovacevic, *A new heat transfer model for friction stir welding*. Transaction of NAMRI/SME, vol. 30 (SME, 2002), pp. 565–572
38. J.E. Gould, Z. Feng, Heat flow model for friction stir welding of aluminum alloys. J. Mater. Process. Manuf. Sci. **7**(2), 185–194 (1998)
39. M. Zahedul, H. Khandkar, J. Khan, Thermal modeling of overlap friction stir welding for Al-alloys. J. Mater. Process. Manuf. Sci. **10**(2), 91–105 (2001)
40. M. Song, R. Kovacevic, Thermal modeling of friction stir welding in a moving coordinate system and its validation. Int. J. Mach. Tools Manuf **43**, 605–615 (2003)
41. Jerry C. Wong, *The Correspondence between Experimental Data and Computer Simulation of Friction Stir Welding (FSW)* (Department of Mechanical and Aerospace Engineering Morgantown, West Virginia, 2008)
42. Y.J. Chao, X. Qi, Thermal and thermo-mechanical modeling of friction stir welding of aluminum alloy 6061-T6. J. Mater. Process. Manuf. Sci. **7**, 215–233 (1998)

43. Y.J. Chao, X. Qi, W. Tang, Heat transfer in friction stir welding—experimental and numerical studies. ASME J. Manuf. Sci. Eng. **125**(1), 138–145 (2003)

44. M. Mehta, A. Arora, A. De, T. Debroy, The minerals. Metals Mater. Soc. ASM Int. (2011). doi:10.1007/s11661-011-0672-5